Journal of Solid State Electrochemistry
https://doi.org/10.1007/s10008-020-04586-2

ORIGINAL PAPER

Introducing a low-cost tool for 3D characterization of pitting corrosion in stainless steel

Dyovani Coelho[1] · Oscar A. Cuadros Linares[2] · Aloadir L. S. Oliveira[1] · Marcos A. S. Andrade Jr[1] · Lucia H. Mascaro[1] · João E. S. Batista Neto[2] · Odemir M. Bruno[2] · Ernesto C. Pereira[1]

Received: 28 November 2019 / Revised: 24 March 2020 / Accepted: 30 March 2020

Abstract

Herein, we propose an approach to three-dimensional (3D) reconstruction of corroded samples to have access to information about the shape, diameter, volume, depth, and spatial distribution of pits. For this purpose, a 304 stainless steel sample, after exposure to controlled corrosion conditions, was submitted to a sequence of polishing, surface image acquisition, and sample thickness measurement. This allows the 3D reconstruction of the sample using computational tomography. The analyses of the two-dimensional and the reconstructed three-dimensional images made it possible to evaluate all the geometric parameters of the pits as well as to compare these data with the electrochemical measurements recorded during the corrosion process.

Keywords Pitting corrosion · 3D reconstruction · Three-dimensional corrosion analysis · Stainless steel

Introduction

Metallic corrosion has a significant impact on society. The loss of lives, negative social impact, and environmental pollution are issues commonly related to accidents resulting from the corrosion of different types of structures. In the world economy, estimates indicate that the cost generated by corrosion is about US$ 2.5 trillion, of which up to 35% could be saved using adequate corrosion control practices [1]. However, the correct choice of the control method is tied to the knowledge of the corrosion mechanism. In this aspect, pitting corrosion on stainless surfaces is extremely worrying, since it is hard to detect, predict, avoid, or even minimize. Pits are formed where a rupture of the passive layer occurs [2–6], such as in inclusions [7–9], intergranular defects [10], or regions with damage in the protective layer [11–14]. In stainless steel and other alloys with a resistant passive film, pits can have several shapes and may be partially covered by insoluble oxides produced during the corrosion process [15, 16]. Figure 1 shows different types of pit shapes. It can be seen that in some of them, such as subsurface, lacy cover, undercutting, and horizontal grain attack, the width at the pit mouth is much smaller than inside it. Consequently, from the data interpretation of commonly used microscopy techniques, it is almost impossible to correctly assess the extent of pits, leading to an underestimation of the corrosion.

Among the common methods for corrosion study are the monitoring of the passive layer thickness and the loss of metallic mass, but none of them can be used to determine the pit shape [17, 18]. Currently, the three-dimensional (3D) study of pitting corrosion is performed using microscopy techniques [9, 19], 3D optical scanner [20, 21], confocal microscopy [22–24], and X-ray microtomography [25–27]. Mascaro et al. [9] and Pereira et al. [19] made in situ analyses coupling optical image acquisition with electrochemical data to study the initial pitting corrosion process in AISI (American Iron and Steel Institute) 1040 steel in Na_2S solution. The authors showed that the formation of elliptical pit growth starts at MnS inclusions and observed two distinct behaviors during electrochemical polarization. The current increase is, at first, due to an increase in the pit area, whereas in the second stage is caused by an expressive increase in the number of small pits. Chen et al. [20] and Kashani et al. [21] studied the corrosion at

Electronic supplementary material The online version of this article (https://doi.org/10.1007/s10008-020-04586-2) contains supplementary material, which is available to authorized users.

✉ Ernesto C. Pereira
ernesto@ufscar.br

[1] Universidade Federal de São Carlos, Rodovia Washington Luís, km 235 SP-310, São Carlos, SP 13565-905, Brazil

[2] Universidade de São Paulo, Av. Trab. São-Carlense, 400 - Parque Arnold Schimidt, São Carlos, SP 13566-590, Brazil

Published online: 16 May 2020

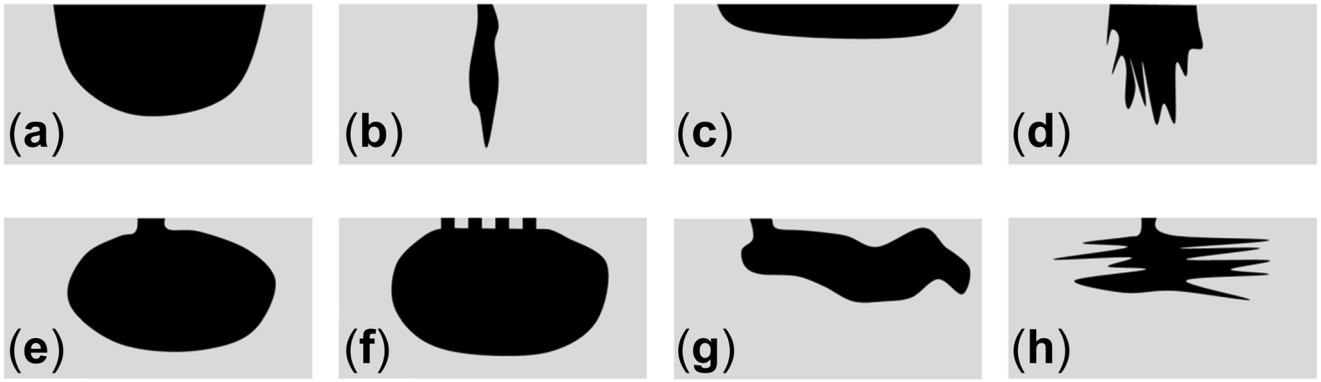

Fig. 1 Representation of the pit shapes. **a** Elliptical, **b** narrow deep, **c** shallow wide, **d** vertical grain attack, **e** subsurface, **f** lacy cover, **g** undercutting, **h** horizontal grain attack (adapted from references [15, 16])

reinforcement steel bars in concrete structures using 3D laser scanner. In both papers, the authors used 3D analysis to reconstruct the surface of the steel bars and to evaluate their cross-sectional area loss. The outcomes of these studies are a set of time-variant probabilistic models of pitting corrosion, which were associated with mass loss. Chen et al. [22, 23] evaluated the corrosion of X80 steel in NaCl solutions by confocal microscopy and concluded that the pits are initiated at mechanical and inclusion defects. Besides, the authors concluded that the pit growth rate decreases with time and inferred that the temperature does not affect on the pit shape but increases the pit growth rate.

Employing the aforementioned techniques—optical microscopy, 3D laser scanning, and confocal microscopy—only the elliptical, narrow deep, shallow wide, and vertical grain attack pit shapes can be detected and described, because these methods focus only on the sample surface.

To investigate subsurface, lacy cover, undercutting, and horizontal grain attack pit shapes, an experimental setup is necessary that puts light on the nature underneath the sample surface. X-ray microtomography tool certainly is a suitable technique to study the inner structure of materials and provides valuable information about the corrosion mechanism beneath the metallic surface. However, this technique requires synchrotron light, which makes it expensive. Hence, few reports on the investigation of corrosion process using X-ray microtomography can be found. Davenport et al. [25, 26] used in situ X-ray microtomography to study pitting corrosion on AISI 304 stainless steel in NaCl solution. The authors found that the pits had a lacy cover shape and the pit propagation is affected by the microstructure, especially the MnS inclusions. In addition, the pitting depth is probably related to the diffusion of ions through the lacy cover, which controls the growth and stability of the pits. In situ X-ray microtomography has also been used by Itty et al. [27] to study the difference of corrosion mechanism in carbon and stainless steel embedded in cement paste. The authors pointed out that corrosion in stainless steel causes greater damage to the cement paste than corrosion in carbon steel. In the first case, pitting corrosion occurs and locally concentrates the corrosion products, which cracked the cement paste cover. In contrast, corrosion in carbon steel is uniform, which led to the formation of corrosion product layer at the steel/cement paste interface. Unfortunately, the use of X-ray microtomography is limited to samples with diameter smaller than 0.5 mm in order to achieve optimal X-ray transmission through steel. In addition, electrodes of this size behave differently due to its relationship with the diffusion layer growth, the mass transport, and the no-uniformity of current density between work and counter electrodes, which depends on the electrochemical cell geometry [28].

Considering these aspects, a framework is proposed that combines computational techniques for 3D reconstruction, optical microscopy, and sample preparation, in order to produce a low-cost method to detect and assess pit corrosion. From a set of sample slices obtained by 2D optical microscopy, uniform and aligned 3D data is produced. This 3D data is processed, allowing the visualization of spatial distribution and shape change of the pits underneath the surface. In addition, 3D view allows the characterization of pit geometry such as size, depth, volume, sectional area, and shape.

Experimental

Electrochemical measurements

AISI 304 steel (Goodfellow – Fe/Cr18/Ni10) wire with 1.0 mm diameter embedded in epoxy resin was used as working electrode. The steel sample was cleaned following ASTM G1-03 (C.7.1) procedure prior to the manufacture of the working electrode [29]. Briefly, the sample was polished using sandpaper 2000 grit, rinsed, and immersed into 10% (vol.) HNO_3 (Labsynth, Brazil) for 20 min at 60 °C. Next, the sample was dried with N_2 gas and embedded in epoxy resin (Polipox, Brazil). After the resin has been properly cured, the surface of the working electrode was polished with

sandpaper 400, 600, 1200, and 2000 grit, followed by the polishing with alumina slurry (1 μm) and cleaning with acetone in ultrasonic bath. The geometric area exposed to the solution was a disc surface with 7.54×10^{-3} cm^2. A counter-electrode of the same stainless steel (AISI 304 steel) was made as a ring surrounding the working electrode and an Ag/AgCl/KCl saturated (Ag/AgCl) was used as reference electrode.

Using a potentiostat/galvanostat Autolab-PGSTAT30 (Metrohm, Switzerland) controlled by the NOVA 1.11 software, a two-step procedure was performed to drive the formation of pit corrosion. First, the open-circuit potential (OCP) was measured for 1 min, and finally 0.46 V vs Ag/AgCl was applied to the working electrode during 10 min. This potential and time were chosen to guarantee the formation of corrosion with characteristics of lacy cover and subsurface shape in a short period since the goal is to develop a method of three-dimensional reconstruction of the corrosion.

The electrochemical experiments were performed with a jacketed one compartment cell at 25 °C, and a 0.1-mol L^{-1} HCl (Labsynth, Brazil) solution was used as electrolyte. All solutions were prepared using water purified with a Milli-Q system (18 MΩ cm), and all reagents were used without further purification.

Images acquisition and 3D reconstruction

Images of the working electrode surface were acquired by an inverted microscope OM model TNM-07T-PL (Anatomic, Brazil) coupled to a camera (DV-500) controlled by the LissView v. 7.1.1.5 (Guangzhou Liss Optical Instrument Co., LTD, China). The 3D reconstruction of the electrode was made once a set of the electrode surface images was acquired by progressive axial sectioning of the sample. The detailed procedure is described below. First, sample surface images were taken. Then, the sample thickness was measured with a digital micrometer (Mitutoyo - Coolant Proof Micrometer Series 293 IP-65) with a resolution of ± 1 μm. After that, the electrode surface was thinned by gently polishing with sandpaper 2000 grit, followed by polishing with alumina slurry (1 μm), always keeping the corroded surface perpendicular to the axial plane of the electrode (Fig. 2). Next, the surface was washed with acetone, after that, with water and dried. Then, a new set of segmented electrode surface images was taken, and the sample thickness was measured again. All these steps of thinning, surface image acquisition, and thickness measurement were repeated until no further pitting corrosion was observed on the electrode.

Corrosion volume reconstruction

A 3D image (volume) was built by stacking up the series of 2D images acquired, in order that each 2D image is a slice of the 3D volume. This process has been largely applied in medical imaging, where 3D data such as computed tomography (CT), magnetic resonance imaging (MRI), and confocal microscopy (CM) are generated from 2D images [30]. Nevertheless, this non-trivial task demands heavy image preprocessing, which involves the analysis of many image features. To eliminate any artifacts in the final 3D volume, prior to the volume reconstruction method itself, each 2D image was processed in order to remove abrasion and scratch marks from the polishing processes. The volume reconstruction method is a fourfold process: (1) slice size standardization; (2) slice alignment; (3) slice interpolation; (4) segmentation.

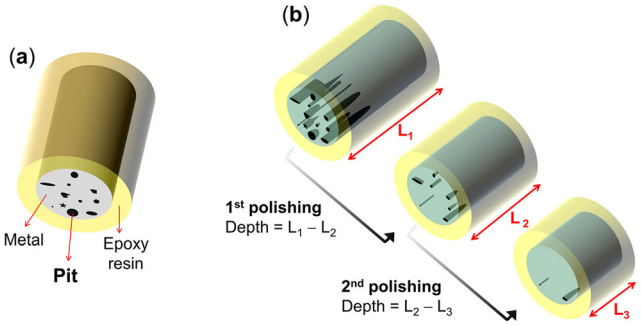

Fig. 2 Representation of the (**a**) electrode embedded in epoxy resin after controlled corrosion procedure, (**b**) direction of slicing and how the polishing depth is calculated

1. To ensure high definition to the surface image acquisition, this process was made using a 10 times magnifying lens. Hence, the examination of small pits was possible; however, the image capture of the whole surface was not feasible. Thus, 2D surface images were initially acquired applying a collage reconstruction technique, which resulted in slices of different sizes (pixels). The size of each slice was padded using the largest as a reference, bringing all 2D images to the same dimensions. This process guarantees that the size and shape of the stainless steel sample (the object under investigation) remain unaltered.
2. All the images were aligned during the stacking up process to correct slight translational or rotational shifts between slices. From a reference slice, an affine image registration method was applied to find a geometric transformation that provides the correct alignment between two slices.
3. An interpolation function was applied to fill out the missing data between two slices, using the known distance measured by the digital micrometer. First, the input slices were stacked in their corresponding position, which generates a volume with empty spaces. Then, the slices surrounding the blanks were used to fill the vacancies by linear interpolation.
4. The generated volume is segmented into three regions: the stainless steel sample, the pitting corrosion, and the background.

All images were processed using the free softwares ImageJ 1.51j8 (Wayne Rasband - National Institutes of Health, USA), ITK-SNAP 3.4.0 (U.S. National Institute of Biomedical Imaging and BioEngineering) [31], and Image Composite Editor 2.0.3.0 (Microsoft Corporation).

To perform the pit count at each electrode slice and analyze the pit evolution, a binarization procedure was performed as described by Zimer et al. [19, 32, 33]. Briefly, the image is converted to grayscale (8 bites), and an intensity threshold is set to delimitate the areas corresponding to pits; thus, the image is binarized making it possible to distinguish objects (pits) from background (AISI 304 steel surface) [19]. It should be noted that a filter was applied so that an object was considered pit only if it had sectional area higher than 7 μm^2.

Results and discussion

To ensure the pitting formation, the corrosion was electrochemically driven by a potentiostatic experiment, applying 300 mV vs Ag/AgCl more positive potential than the pit potential determined by cyclic polarization curve [34] (Supplementary Information S1). Images of the electrode surface before and after polarization are shown in Fig. 3, in which many corrosion spots with variable diameters can be seen at the end of the chronoamperometric procedure. The potentiostatic polarization curve for the SS-1 (Stainless Steel-1) electrode is also presented in Fig. 3. The potentiostatic current transient and surface images of the SS-2 (Stainless Steel-2) electrode, investigated under the same experimental conditions, are shown in Supplementary Information S2. The SS-1 and the SS-2 are the same kind of sample and were analyzed for getting information on the reproducibility and reliability of the method. After a sharp current increase related to the beginning of the potential application, a current diminishing from 60 to 75 s is observed. This decrease is due to the growth of a passive film that remains in the electrode surface and prevents the local oxidation. This passive layer is composed of oxides, hydroxides, and oxyhydroxides, especially NiO and Cr_2O_3, which are expected to be partially insoluble in acidic medium [35] [5], even if the near-surface pH is more acidic than the bulk electrolyte [36]. From 75 s, the potentiostatic current transient shows that the current increases more smoothly up to 600 s, since the applied potential is sufficient to initiate and maintain the pitting corrosion process. The stable pit formation rate may be related to the high solubility of hydrated nickel oxide compared with hydrated chromium oxide, leading to selective dissolution of the passive film and production of a chromium-rich layer on the surface [2]. Microstructural defects avoid the formation of a homogeneous passive layer so that pitting corrosion nucleation occurs from the localized rupture of the passive film in these defects, such as metal grain boundaries,

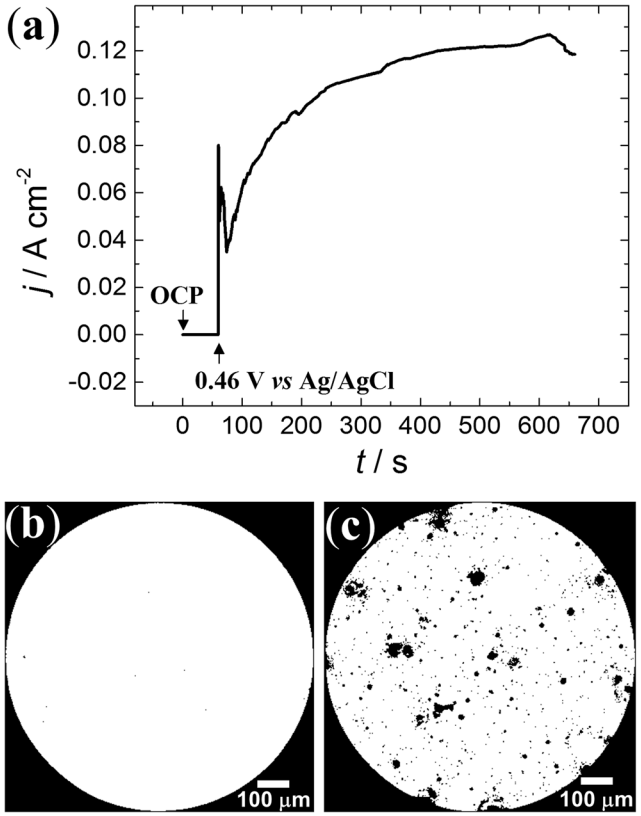

Fig. 3 (**a**) Potentiostatic current transient to SS-1 electrode in 0.1 mol L^{-1} HCl at 25 °C and optical microscopy images of the electrode surface (**b**) before and (**c**) after polarization at 0.46 V vs Ag/AgCl during 600 s

interfaces between metal bulk and inclusions, and presence of secondary phase particles [4, 19]. The surface area increases as soon as cavities are created, and associated with that the pH decreases inside these pits due to the low proton diffusion to the bulk electrolyte, promoting the dissolution of chromium oxides. These events make the corrosion more aggressive and the current flow increases again, leading to pit growth under the electrode surface, which will be evaluated hereafter.

Based on the electric charge associated with the current obtained from the potentiostatic polarization experiments (Fig. 3), it was possible to calculate the mass of oxidized material, which were 1.30×10^{-4} g (0.48 *C*) and 1.00×10^{-4} g (0.37 *C*) for SS-1 and SS-2, respectively. Besides Faraday's law, some assumptions were made to calculate the mass of oxidized material: (1) the AISI 304 steel is composed of 72% Fe, 10% Ni, and 18% Cr; (2) at the electrolyte pH and applied potential the chemical species produced are Fe^{2+}, Ni^{2+}, and Cr^{3+}; and (3) the current only flows through the pits and with a 100% faradaic current efficiency [37]. Since the crystal structure of AISI 304 steel consists of austenite with fcc structure and lattice parameter 0.361 nm [38], the sample density can be estimate as 7.830 g cm^{-3}. Based on the estimated density and oxidized mass values (1.30×10^{-4} g to SS-1 and 1.00×10^{-4} g to SS-2 electrode), the total corrosion volume can be calculated, which are 16.6×10^6 μm^3 and

12.8×10^6 μm^3 for SS-1 and SS-2 samples, respectively. This information will be useful to compare with the corroded volume caused by the 3D reconstruction.

Figure 4 presents some slices of the segmented corroded SS-1 electrode, including the electrode surface. The corroded portion of the electrode can be split into three distinct regions: (1) the shallow region, up to 16 μm; (2) an intermediary region from 16 to 91 μm; and (3) the deep region, from 91 μm to the bottom of the pits. A similar figure for the SS-2 electrode is shown in the Supplementary Information S3.

From the observation of different regions in the sample, some important features can be highlighted. It can be generalized that the number of small pits is much higher than that of large pits, although it is observed that the smallest are shallow and thin. In the shallow region, it can be seen that the number of pits increases from 158 to 590 when comparing the surface with the region 3 μm deeper in the electrode. This is because some of the subsurface pits have such a small opening that they can be considered hidden pits, which are revealed once the scrap process is initiated. It can also be pointed out that many of the small pits in the shallow region increase in diameter as they deepen, and some of them collapse with larger pits in the vicinity. For this reason, the largest pits are exposed only after axial slicing of the electrode with polishing, a characteristic of lacy cover and subsurface pits. Thus, the methodology employed here allows identifying and estimating even hidden pits, since the pit nucleus has dimensions in the detection range of the optical microscope. In the intermediate region, the shallow pits disappear, and it can identify 10 large pits with no abrupt change in the elliptical shape. Following in the deep region, the bottom of each large pit reveals the most striking feature of this analysis. There are patterns of many individual small pits that form a root-like structure. While neighboring wells collapse and the corrosion continues on the surface, individual wells are deepening at the bottom. In the studies of Davenport et al. [25, 26], similar patterns were observed, but only to galvanostatic control. According to the authors, this growth structure as etched perimeter stems from the cracking of the saline layer that passivates the bottom of the pit. Here, it is not possible to state that the bottom of the pits is a vertical grain attack because the microstructure of this region (underneath the surface) is hard to investigate. On the other hand, the slices of the deep region show that here the same type of pit growth is observed, even with potentiostatic control.

To complement the afore-discussed results, Fig. 5 shows the evolution of pits growth based on the frequency of pits as a function of the sectional area and of the slice depth. The circle area refers to the frequency of pits with the same sectional area variation at a given slice depth, and the centers of each circle

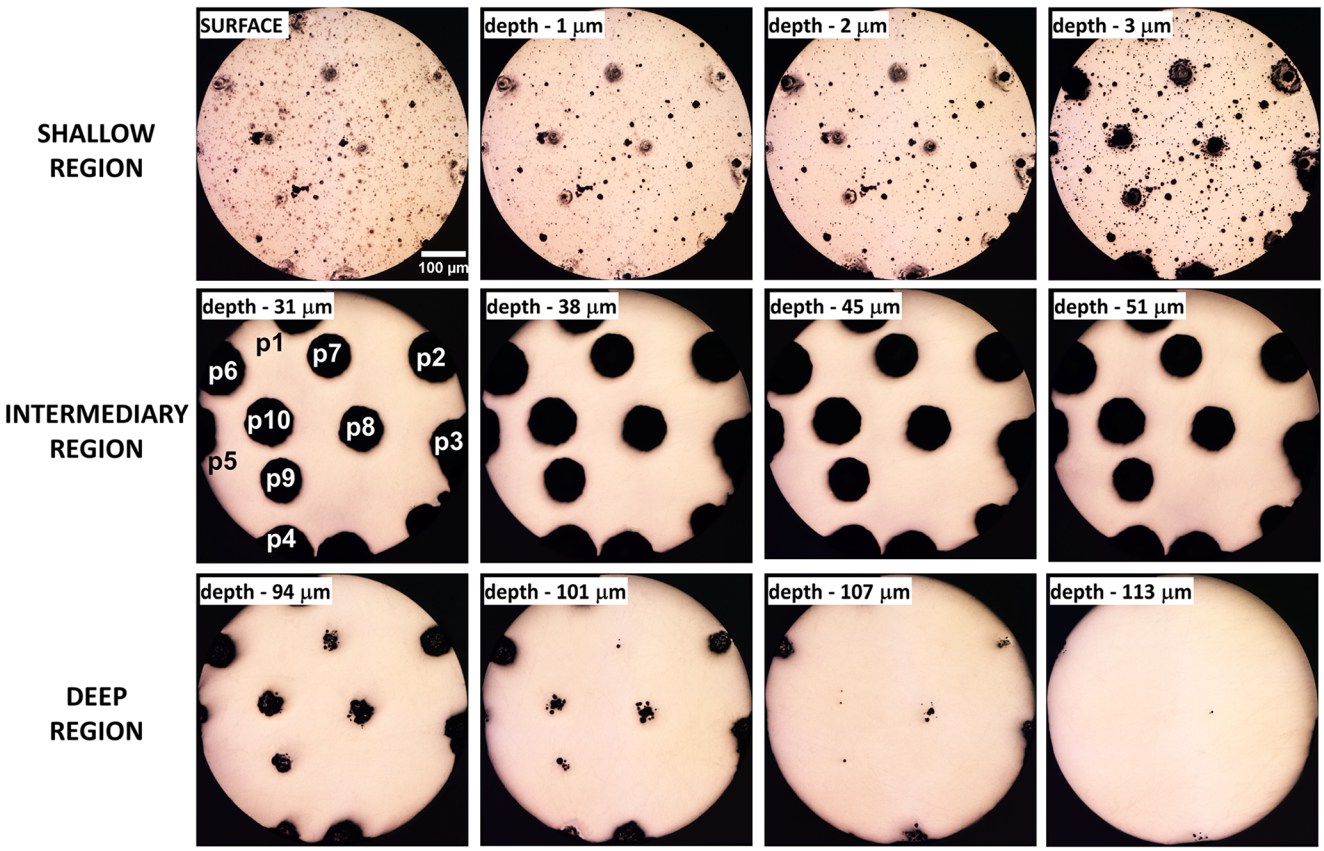

Fig. 4 Image series of the SS-1 corroded electrode at different depths. All images have the same resolution and magnification

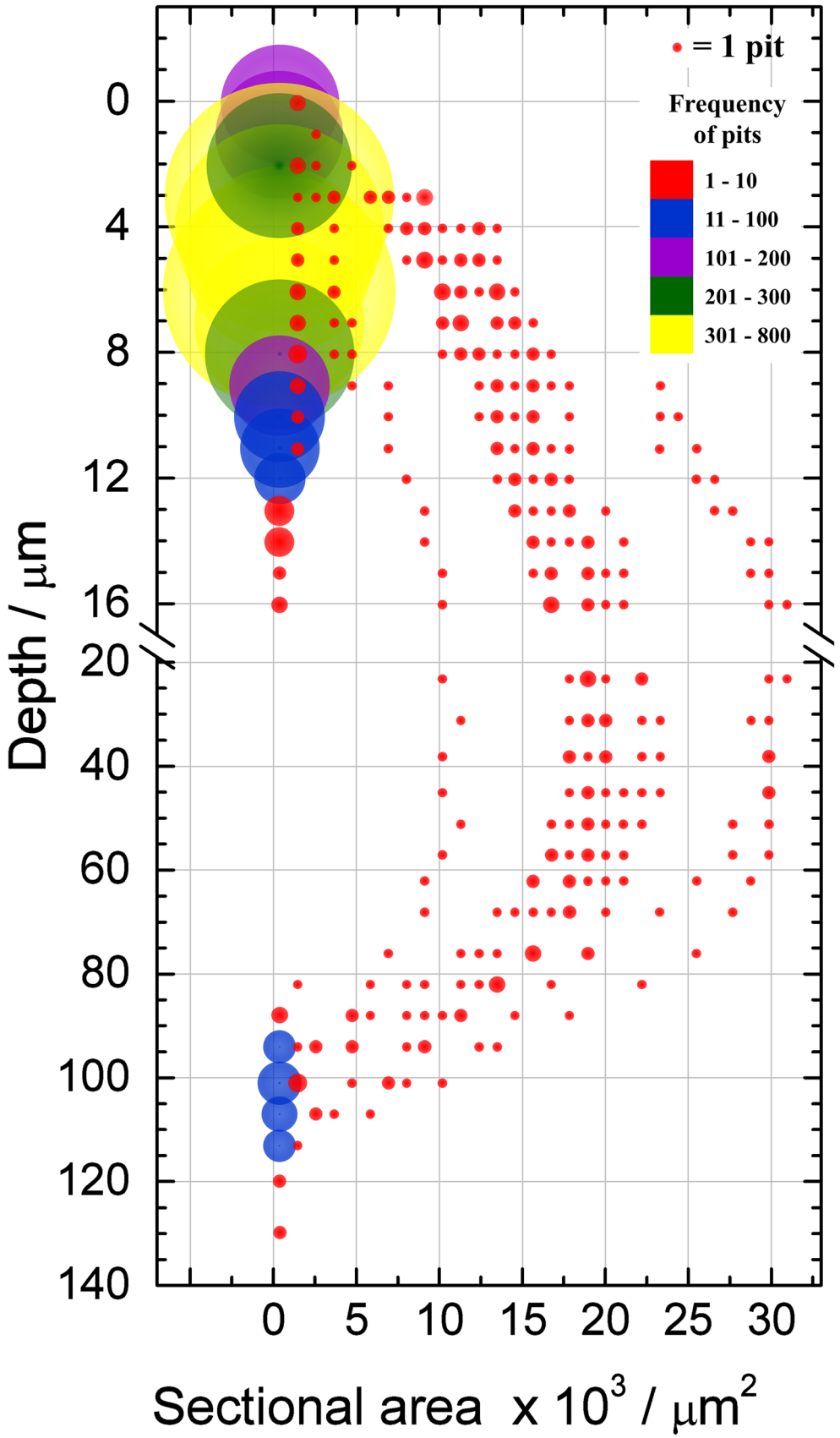

Fig. 5 Sectional area and frequency of the pits as a function of the slice depth to SS-1 sample (SS-2 is shown in the Supplementary Information S4). The area of circles is proportional to the frequency of pits. For best visualization, the frequency of pits is classified in a range of colors too

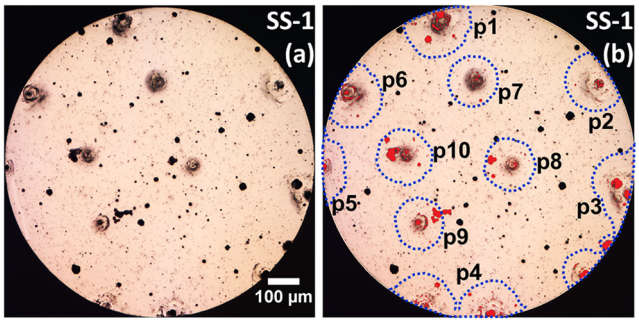

Fig. 6 The first slice of the segmented images showing the (**a**) bare surface and (**b**) the projection of the maximum sectional area of the larger pits in the SS-1 sample (dashed blue lines) with the openings of the pit identified in red (SS-2 is shown in the Supplementary Information S5). The images have the same resolution and magnification

are positioned according to the variation of pit-sectional area, considering an amplitude variation of 1091 μm^2. It can be seen that there is a large number of small pits in the first slices; however, the sectional area of the pits increases as their frequency decreases in deeper regions. This happens because neighboring shallow pits collapse into large pits, which reflects the frequency-lowering behavior of pits with low-sectional area from 4 to 16 μm deep. It is noteworthy that the collapse of large pits is identified only by slicing the electrode once this phenomenon cannot be visualized by surface analysis.

Another interesting feature of this methodology is that it allows following the evolution of large pits, and three patterns of increase in the sectional area can be identified. The first is the collapse of large pits from 9 μm depth producing the two highest sectional area pits, identified as p3 and p4 in Fig. 4. The second pattern refers to pit p5, the only large pit that is deep but present the lowest sectional area in the intermediary region. Finally, the third pattern is observed for the evolution of the other large pits, which are deep and do not collapse with each other. The sectional area of large pits gradually increases up to 23 μm depth and remains almost constant up to 51 μm depth. Also, the frequencies of pits with a specified sectional area in this region hardly change. Furthermore, from 51 to 88 μm depth, the sectional area of the large pits decreases continuously until the bottom of the pits is reached. In this deeper region, the frequencies of pits with small-sectional area increase due to the exposure of the "roots" of the large pits, confirming what was afore-discussed.

The series of axial images in Fig. 4 and the frequency profile of large pits in Fig. 5 show the presence of 10 large pits at 31 μm depth for SS-1 sample. All of these large pits can be classified as lacy cover. The same analysis shows 9 large pits in the corroded SS-2 sample (Supplementary Information S5). According to the model proposed by Laycock et al. [39], the formation of pits with lacy cover depends on the dissolution rate of metal and the diffusion of metal ions out of the pit. Then, the number of openings and their sectional area should affect both factors, once the ohmic drop and the diffusion resistance are affected by the ion flow through the lacy cover. By identifying the openings of large pits (red) and marking them at the surface slice, many small openings are observed tens of micrometers from the center of the pit and from its main opening (Fig. 6). The methodology used to find the openings and channels of the large pits is described in the Supplementary Information S6. The maximum-sectional area of the pits is shown as dashed blue lines in Fig. 6. These small openings are called channels once they are not situated in the region of lacy cover; i.e., they remain as individual pits at the beginning of the corrosion process, but at some point, they collapse with the large pit at a minimum depth of 4 μm. This can be explained because the channels could act as an alternative way for the diffusion of ions through the pit, which keeps the pit growth stable without collapsing with the lacy cover. If the 3D reconstruction technique was not used, these channels would hardly be identified as belonging to the same pit.

The number of openings and channels for all large pits identified in samples SS-1 and SS-2 is shown in Tables 1 and 2, respectively. At the sample SS-1, except the p5 pit, the other large pits present at least one

Table 1 Openings and channels from analyses of 3D reconstruction of the large pits in SS-1 electrode

ID	p1	p2	p3	p4	p5	p6	p7	p8	p9	p10
Pit openings	92	89	122	172	52	94	72	84	63	75
Number of channels*	6	4	7	4	0	1	2	4	4	3
Sectional area of each channel (μm^2)	13; 16; 19; 40; 60; 340	11; 15; 25; 33	14; 14; 15; 15; 39; 45; 65	12; 41; 78; 155		29	10; 49	17; 20; 94; 405	10; 60; 199; 523	16; 68; 160

* Channels with sectional area higher than 10 μm^2

Table 2 Openings and channels from analyses of 3D reconstruction of the large pits in SS-2 electrode

ID	p1	p2	p3	p4	p5	p6	p7	p8	p9
Pit openings	58	149	18	20	72	72	47	92	63
Number of channels*	4	5	0	0	2	5	0	2	2
Sectional area of the channels (μm^2)	14; 15; 18; 164	11; 12; 15; 24; 26			26; 377	12; 18; 39; 78; 78		58; 103	22; 90

* Channels with sectional area higher than 10 μm^2

channel with a sectional area higher than 10 μm^2. No clear correlation is seen among the number of openings, the number of channels, and the sectional areas; however, the presence of the channels along with the large sectional area of the pit with the main opening may be related to the pit corrosion volume. Unfortunately, optical microscopy is not accurate enough to determine the sectional area of the pores at the surface of the lacy cover pits, hindering further discussion.

Without the methodology applied to 3D reconstruction, it would not be possible to evaluate the characteristics observed near the electrode surface and at the bottom of the pit. Common methods for evaluating corroded samples are based on microscopy techniques—as SEM (scanning electron microscopy) and AFM (atomic force microscopy)—and only allow the evaluation of the electrode surface. On the other hand, 3D reconstruction of the electrode provides a detailed characterization of pitting corrosion and allows the analysis of individual pits. In this way, after 3D reconstruction of the electrode volume, the lacy cover elliptical shape best describes the large pits in the SS-1 and SS-2 samples, as seen in the sagittal and coronal segmentations of 3D reconstruction in the Fig. 7. The arrow in the cylindrical 3D projection at each segmentation view shows the vision direction while the red cut plane shows the image plane exhibited at each segmentation view.

Figure 8 shows the 3D reconstruction of the SS-1 electrode, where the pit opening is shown in red, and the pit volume inside the electrode is shown in black. It is clearly that all large pits have a small opening compared with their maximum pit radius. Moreover, the 3D reconstruction of the SS-1 and SS-2 electrodes shows 609 and 338 pits, respectively. These numbers were counted considering that representative pits are those with diameter and depth higher than 3 μm and volume higher than 23 μm^3. Although there are a large number of pits, there are few with large volumes, which agrees with the analyses of frequency of the sectional areas as a function of the slice depth in Fig. 5. The image reconstruction shows that all pits present elliptical shape, although the small ones are classified as subsurface while the large ones are lacy cover type [32]. Furthermore, once the electrode volume is segmented, the geometric parameters such as pit volume can be calculated. Thus, the total corroded volume of the SS-1 and SS-2 electrodes was 17.1×10^6 μm^3 and 14.5×10^6 μm^3, respectively. These values are in agreement with those calculated by electrochemical analysis (16.6×10^6 μm^3 and 12.8×10^6 μm^3 for SS-1 and SS-2 samples, respectively), differing by 3.01% for SS-1 and 13.6% for SS-2. The overestimation of the 3D data may be a result of the polishing process or the chemical corrosion inside the pit, which could increase the volume of pits without generating electric current. Moreover, inside the

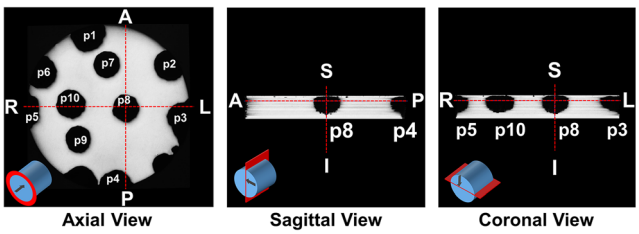

Fig. 7 Images of SS-1 volume from ITK-Snap showing the slices with *XYZ* coordinates (1258 - 1083 - 67) and axial, sagittal, and coronal view of the 3D reconstruction. The chart at lower left in each image (blue cylindrical projection) represents a wire, while a red blade and the black arrow represent the point of view

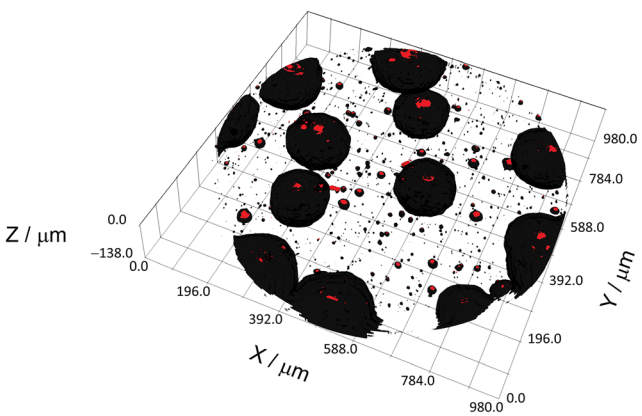

Fig. 8 3D pitting reconstruction of the SS-1. Red corresponds to the openings of the pits seen in the tilt of the image. Black is the pitting underneath the surface of electrode (3D reconstruction of SS-2 is shown in Supplementary Information S7)

Table 3 Measured parameters associated to the large pits for SS-1 and SS-2 electrodes

	ID*	p1	p2	p3	p4	p5	p6	p7	p8	p9	p10
SS-1	Pit volume ($\times 10^6$ μm^3)	1.81	1.53	2.15	2.32	0.70	1.53	1.26	1.39	1.26	1.59
	Depth (μm)	113	107	113	113	113	113	101	113	107	107
	Sa_{max} ($\times 10^4$ μm^2)**	2.23	2.02	2.98	2.92	1.02	1.98	1.91	1.93	1.86	2.26
SS-2	Pit volume ($\times 10^6$ μm^3)	1.66	3.49	0.61	0.15	1.74	1.84	1.39	1.74	1.72	
	Depth (μm)	131	126	161	57	118	118	126	126	126	
	Sa_{max} ($\times 10^4$ μm^2)	1.88	4.51	0.70	0.41	2.14	2.29	1.76	2.21	2.23	

* ID, identification of the pit (the large pits at SS-1 are identified in the Fig. 7)

** Sa_{max}, maximum sectional area of the pit

pit, the electrode-solution interface can build up anodic-cathodic zone, which could lead to self-corrosion, and the image corrosion size must be larger than the polarization corrosion measured. This anodic-cathodic zone could arise in MnS inclusions, as demonstrated by Krawiec et al. [40] using the scanning vibrating electrode technique to study the dissolution and pitting corrosion at MnS inclusions. The authors show that the MnS could behave as a cathodic zone while the bare metal works as an anodic zone. Also, Zimer et al. [9] show that the formation of pitting corrosion on AISI 1040 steel starts to grow in inclusion of MnS, even keeping the sample under open-circuit potential.

3D reconstruction also confirms that in the SS-1 electrode, it is possible to identify 10 large pits with volume higher than 0.1×10^6 μm^3. These 10 pits correspond to 90.6% (15.5×10^6 μm^3) of the total pit volume computed after 3D reconstruction. The same behavior is observed in the SS-2 electrode where the 9 largest pits correspond to 99.3% (14.4×10^6 μm^3) of total pit volume. These characteristics, as well as the volume, depth, and maximum sectional area of the large pits, are summarized in Table 3. The pits with the highest volume are the result of coalescence of large pits inside the electrode. In the SS-1 electrode, p3 and p4 are the two pits produced by this mechanism, while the SS-2 sample presents only the pit p2 as a result of large pits coalescence. This is a remarkable outcome provided by the 3D reconstruction methodology to study pit corrosion: a low-cost technique that allows the identification of coalescence among pits, a process that is hard to detect by other techniques once it occurs below the sample surface. In the Supplementary Information, there are videos showing the 3D view of the SS-1 sample reconstructed (Supplementary Information S8) and the 3D view showing only the pits to the SS-1 sample (Supplementary Information S9).

In contrast, by restricting the comparison only to large pits that do not coalesce, pit p6 in the SS-1 sample has the largest number of openings and yet does not have the largest volume, even though it is one of the deepest. The same trend is observed in the SS-2 electrode, where the pit p8 shows the highest number of openings but not the highest volume. Despite no correlation between the pit volume and the number of openings, the volume seems to be tied to the presence of the channels. The pits with the lowest volume are p5 and p3 in SS-1 and p4 and p7 in SS-2 sample, in which the absence of channels is a common feature.

The overlap of 2D images, keeping the same position of electrode during the acquisition of segmented images, allows to identify the growth of pits and then their individualization. Thus, the identification (ID) of the pits in a 3D coordinate allows its visualization in detail. It is remarkable that the 3D reconstruction is in agreement with the tomograms obtained by Ghahary et al. [25, 26] in situ X-ray microtomography of pitting corrosion of AISI 304 steel study, even using a low-cost methodology to do that. However, the authors use a very expensive experimental apparatus in the TOMCAT (TOmographic Microscopy and Coherent rAdiology experimenTs, Swiss Light Source, Villigen, Switzerland) beamline synchrotron X-ray source. Notwithstanding, the use of the X-ray microtomography is a non-destructive technique for 3D analysis; the size of sample is very limited, which increases the border effect in electrochemical experiments. On the other hand, the methodology proposed here can be used at samples with a large diameter (the wires of stainless steel used here were 1.0 mm of diameter).

In short, besides the relatively inexpensive apparatus employed, the 3D reconstruction methodology makes it possible to study the pit shape and to obtain volume, opening, spatial distribution, and depth metrics. Also, the 3D reconstruction shows good agreement with the electrochemical data since the total corrosion volume matches with the corrosion charge. The main points that come after these analyses are the disclosure of small hidden pits, the coalescence among large pits underneath the electrode surface, and the exposure of "roots" and channels in the large pits, which certainly deserve detailed investigations.

Conclusions

For the first time, 3D reconstruction of the corrosion volume using optical images has been demonstrated, allowing detailed analyses of the shape and distribution of the pits. The methodology employed in electrode reconstruction after the corrosion process showed remarkable agreement with the electrochemical data. For SS-1 and SS-2 samples, respectively, an overestimation of about 3.01% and 13.6% is observed between the 3D model and the electrochemical data, which is expected due to the required sample polishing process. Moreover, 3D reconstruction shows that small pits have a subsurface and elliptical shape, while large pits have lacy cover elliptical shape. Still about large pits, some remarkable results can be highlighted: at the top, it was channels whose roles in corrosion process are not yet clearly understood; at the bottom, a pattern of many small pits was shown, as "roots." As the mechanism that originates these "roots" was not investigated, a deeper discussion involving corrosion by grain or interstitial attack would be rash. In fact, from 3D reconstruction using optical microscopy allied with computational tools, as described here, it is possible to investigate the pit formation in many different substrates and conditions, with an unprecedented acquisition of detailed information.

Funding information This work was supported by FAPESP (Grant 2013/07296-2), CNPq, and the Coordenação de Aperfeiçoamento de Pessoal de Nível Superior - Brasil (CAPES) - Finance Code 001.

Compliance with ethical standards

Conflict of interest The authors declare that they have no conflict of interest.

References

1. Koch G, Varney J, Thompson N, Moghissi O, Gould M, Payer J (2016) International measures of prevention, application, and economics of corrosion technologies study. Houston, Texas, USA
2. Marcus P, Grimal JM (1992) The anodic dissolution and passivation of NiCrFe alloys studied by ESCA. Corros Sci 33:805–814
3. Olefjord I (1985) Surface composition of stainless steels during anodic dissolution and passivation studied by ESCA. J Electrochem Soc 132:2854
4. Marcus P, Maurice V, Strehblow HH (2008) Localized corrosion (pitting): a model of passivity breakdown including the role of the oxide layer nanostructure. Corros Sci 50:2698–2704
5. Maurice V, Yang WP, Marcus P (1994) XPS and STM investigation of the passive film formed on Cr(110) single-crystal surfaces. J Electrochem Soc 141:3016
6. Pan C, Liu L, Li Y, Wang S, Wang F (2011) Passive film growth mechanism of nanocrystalline 304 stainless steel prepared by magnetron sputtering and deep rolling techniques. Electrochim Acta 56: 7740–7748
7. Zhang W, Frankel GS (2003) Transitions between pitting and intergranular corrosion in AA2024. Electrochim Acta 48:1193–1210
8. Jun J, Holguin K, Frankel GS (2014) Pitting corrosion of very clean type 304 stainless steel. CORROSION 70:146–155
9. Zimer AM, De Carra MAS, Rios EC, Pereira EC, Mascaro LH (2013) Initial stages of corrosion pits on AISI 1040 steel in sulfide solution analyzed by temporal series micrographs coupled with electrochemical techniques. Corros Sci 76:27–34
10. Rios EC, Zimer AM, Pereira EC, Mascaro LH (2014) Analysis of AISI 1020 steel corrosion in seawater by coupling electrochemical noise and optical microscopy. Electrochim Acta 124:211–217
11. Finšgar M, Jackson J (2014) Application of corrosion inhibitors for steels in acidic media for the oil and gas industry: a review. Corros Sci 86:17–41
12. Wadhwani PM, Ladha DG, Panchal VK, Shah NK (2015) Enhanced corrosion inhibitive effect of p-methoxybenzylidene-4, 4′-dimorpholine assembled on nickel oxide nanoparticles for mild steel in acid medium. RSC Adv 5:7098–7111
13. Ait Albrimi Y, Ait Addi A, Douch J, Souto RM, Hamdani M (2015) Inhibition of the pitting corrosion of 304 stainless steel in 0.5 M hydrochloric acid solution by heptamolybdate ions. Corros Sci 90: 522–528
14. Kesavan D, Gopiraman M, Sulochana N (2012) Green inhibitors for corrosion of metals: a review. Chem Sci Rev Lett 1: CS10204205
15. NACE International (2018) Pitting corrosion. https://www.nace.org/Pitting-Corrosion/. Accessed 5 Jul 2018
16. Bhandari J, Khan F, Abbassi R, Garaniya V, Ojeda R (2015) Modelling of pitting corrosion in marine and offshore steel structures - a technical review. J Loss Prev Process Ind 37:39–62
17. ASTM (1990) ASTM G31-72 (2004): Standard practice for laboratory immersion corrosion testing of metals
18. ASTM (2018) ASTM G96-90 (2018): Standard guide for on-line monitoring of corrosion in plant equipment (electrical and electrochemical methods)
19. Zimer AM, Rios EC, Mascaro LH, Pereira EC (2011) Temporal series micrographs coupled with polarization curves to study pit formation under anodic polarization. Electrochem Commun 13: 1484–1487
20. Tang F, Lin Z, Chen G, Yi W (2014) Three-dimensional corrosion pit measurement and statistical mechanical degradation analysis of deformed steel bars subjected to accelerated corrosion. Constr Build Mater 70:104–117
21. Kashani MM, Crewe AJ, Alexander NA (2013) Use of a 3D optical measurement technique for stochastic corrosion pattern analysis of reinforcing bars subjected to accelerated corrosion. Corros Sci 73: 208–221
22. Wang Y, Cheng G (2016) Quantitative evaluation of pit sizes for high strength steel: electrochemical noise, 3-D measurement, and image-recognition-based statistical analysis. Mater Des 94:176–185
23. Wang Y, Cheng G, Li Y (2016) Observation of the pitting corrosion and uniform corrosion for X80 steel in 3.5 wt.% NaCl solutions using in-situ and 3-D measuring microscope. Corros Sci 111:508–517
24. Xu Y, Li H, Li S, Guan X, Lan C (2016) 3-D modelling and statistical properties of surface pits of corroded wire based on image processing technique. Corros Sci 111:275–287
25. Ghahari SM, Davenport AJ, Rayment T, Suter T, Tinnes JP, Padovani C, Hammons JA, Stampanoni M, Marone F, Mokso R (2011) In situ synchrotron X-ray micro-tomography study of pitting corrosion in stainless steel. Corros Sci 53:2684–2687
26. Ghahari M, Krouse D, Laycock N, Rayment T, Padovani C, Stampanoni M, Marone F, Mokso R, Davenport AJ (2015) Synchrotron X-ray radiography studies of pitting corrosion of stainless steel: extraction of pit propagation parameters. Corros Sci 100:23–35
27. Itty P-A, Serdar M, Meral C, Parkinson D, MacDowell AA, Bjegović D, Monteiro PJM (2014) In situ 3D monitoring of corrosion on carbon steel and ferritic stainless steel embedded in cement paste. Corros Sci 83:409–418

28. Stulík K, Amatore C, Holub K, Marecek V, Kutner W (2000) Microelectrodes. Definitions, characterization, and applications (technical report). Pure Appl Chem 72:1483–1492
29. ASTM (2003) ASTM G1-03 (2017): Standard practice for preparing, cleaning, and evaluating corrosion test
30. Angelopoulou A, Psarrou A, Garcia-Rodriguez J, Orts-Escolano S, Azorin-Lopez J, Revett K (2015) 3D reconstruction of medical images from slices automatically landmarked with growing neural models. Neurocomputing 150:16–25
31. Yushkevich PA, Piven J, Hazlett HC, Smith RG, Ho S, Gee JC, Gerig G (2006) User-guided 3D active contour segmentation of anatomical structures: significantly improved efficiency and reliability. Neuroimage 31(3):1116–1128
32. Zimer AM, Rios EC, Mendes P d CD, Gonçalves WN, Bruno OM, Pereira EC, Mascaro LH (2011) Investigation of AISI 1040 steel corrosion in H 2S solution containing chloride ions by digital image processing coupled with electrochemical techniques. Corros Sci 53: 3193–3201
33. Zimer AM, De-Carra MAS, Mascaro LH, Pereira EC (2014) Temporal series of micrographs coupled with electrochemical techniques to analyze pitting corrosion of AISI 1040 steel in carbonate and chloride solutions. Electrochim Acta 124:143–149
34. Amin MA, Abd El Rehim SS, El-Lithy AS (2010) Pitting and pitting control of Al in gluconic acid solutions - polarization, chronoamperometry and morphological studies. Corros Sci 52: 3099–3108
35. Vicente F, Gregori J, García-Jareño JJ, Giménez-Romero D (2005) Cyclic voltammetric generation and electrochemical quartz crystal microbalance characterization of passive layer of nickel in a weakly acid medium. J Solid State Electrochem 9:684–690
36. da Silva MM, Mascaro LH, Pereira EC, Zimer AM (2016) Near-surface solution pH measurements during the pitting corrosion of AISI 1020 steel using a ring-shaped sensor. J Electroanal Chem 780:379–385
37. Takeno N (2005) Atlas of eh-pH diagrams. Intercomparison of thermodynamic databases
38. Zhang HW, Hei ZK, Liu G, Lu J, Lu K (2003) Formation of nano-structured surface layer on AISI 304 stainless steel by means of surface mechanical attrition treatment. Acta Mater 51:1871–1881
39. Laycock NJ, White SP, Noh JS, Wilson PT, Newman RC (1998) Perforated covers for propagating pits. J Electrochem Soc 145:1101
40. Krawiec H, Vignal V, Oltra R (2004) Use of the electrochemical microcell technique and the SVET for monitoring pitting corrosion at MnS inclusions. Electrochem Commun 6:655–660